Review of Scientific Instruments

SpraySyn—A standardized burner configuration for nanoparticle synthesis in spray flames

Cite as: Rev. Sci. Instrum. **90**, 085108 (2019); https://doi.org/10.1063/1.5090232
Submitted: 25 January 2019 • Accepted: 19 July 2019 • Published Online: 23 August 2019

F. Schneider, S. Suleiman, J. Menser, et al.

View Online Export Citation CrossMark

ARTICLES YOU MAY BE INTERESTED IN

Direct numerical simulations of nanoparticle formation in premixed and non-premixed flame-vortex interactions
Physics of Fluids **32**, 093605 (2020); https://doi.org/10.1063/5.0020979

Design and characterization of a linear Hencken-type burner
Review of Scientific Instruments **87**, 115114 (2016); https://doi.org/10.1063/1.4967491

A small porous-plug burner for studies of combustion chemistry and soot formation
Review of Scientific Instruments **88**, 125106 (2017); https://doi.org/10.1063/1.5016212

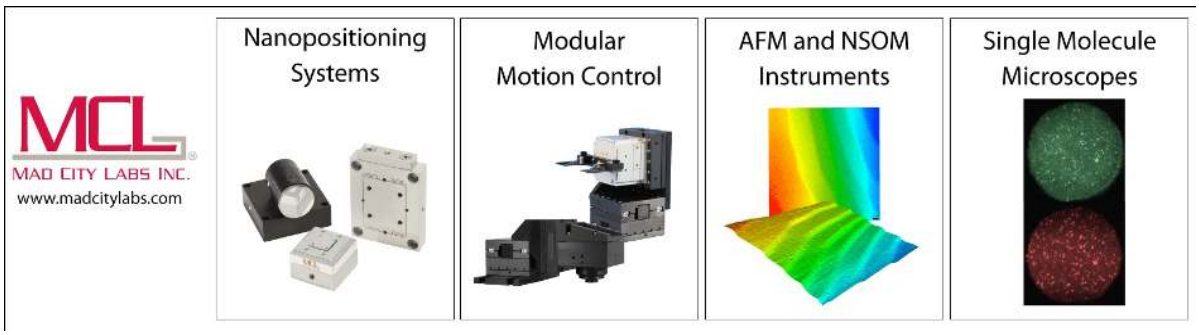

© 2019 Author(s).

Review of Scientific Instruments | ARTICLE | scitation.org/journal/rsi

SpraySyn—A standardized burner configuration for nanoparticle synthesis in spray flames

Cite as: Rev. Sci. Instrum. 90, 085108 (2019); doi: 10.1063/1.5090232
Submitted: 25 January 2019 • Accepted: 19 July 2019 •
Published Online: 23 August 2019

View Online Export Citation CrossMark

F. Schneider,[1,a)] S. Suleiman,[1] J. Menser,[1] E. Borukhovich,[2] I. Wlokas,[2,3] A. Kempf,[2,3] H. Wiggers,[1,3] and C. Schulz[1,3]

AFFILIATIONS

[1]IVG, Institute for Combustion and Gas Dynamics–Reactive Fluids, University of Duisburg-Essen, 47057 Duisburg, Germany
[2]IVG, Institute for Combustion and Gas Dynamics–Fluid Dynamics, University of Duisburg-Essen, 47057 Duisburg, Germany
[3]CENIDE, Center for Nanointegration Duisburg-Essen, University of Duisburg-Essen, 47057 Duisburg, Germany

[a)]**Author to whom correspondence should be addressed:** florian.schneider@uni-due.de

ABSTRACT

In many scientific communities, the definition of standardized experiments has enabled major progress in process understanding. The investigation of the spray-flame synthesis of nanoparticles at a well-defined standard burner by experiment and simulation makes it possible to produce a comprehensive data set with various established and novel measuring methods. In this work, we introduce the design of the SpraySyn burner as a new standard for a free-jet type burner that offers well-defined and simulation-friendly boundary conditions and geometries as well as accessibility for optical diagnostics. A combustible precursor solution is fed through a centrally located capillary and aerosolized with an oxygen dispersion gas flow. The spray flame is stabilized by a premixed flat methane/oxygen pilot flame fed via a porous bronze matrix surrounded by a stabilizing nitrogen coflow emanating through the same porous matrix, providing easy-to-calculate boundary conditions for simulations. This burner design enables the use of a wide choice of solvents, precursors, and precursor combinations. Best-practice operating instructions and parameters are given, and large-eddy simulations are performed demonstrating the suitability of the SpraySyn burner for computational fluid dynamics simulations. For ensuring reproducible operation across labs, we define a consumer-camera-based flame characterization scheme for the quantitative assessment of the flame geometry such as flame length, diameter, tilt angle, and photometric distribution of visible chemiluminescence along the center axis. These parameters can be used for benchmarking the pilot and spray flame by each user of the SpraySyn burner with the reference flames.

© 2019 Author(s). All article content, except where otherwise noted, is licensed under a Creative Commons Attribution (CC BY) license (http://creativecommons.org/licenses/by/4.0/). https://doi.org/10.1063/1.5090232

I. INTRODUCTION

The synthesis of nanoparticulate materials in flames is well-established.[1–4] High-temperature processes enable the generation and stabilization of materials outside the thermodynamic stability limits, and the continuous operation enables scale-up to large production rates as demonstrated for commodities such as silica and titania burners.[1] The synthesis of a large variety of materials has been demonstrated on the lab scale, but conventional gas-phase processes require precursors that are either gaseous or can be vaporized and mixed with the burner gases before they react inside the reaction chamber. Such precursors are only available for a limited number of elements and are often based on metal chlorides, metal organics, and organometallics that tend to be expensive and/or toxic.

Spray-flame synthesis was first proposed by Sokolowski for synthesizing alumina particles from finely sprayed aluminum acetylacetonate solutions[5] and has been extensively developed by Pratsinis, Mädler, and co-workers[6–9] for the production of functional nanoparticles in a wide compositional range. Nonvolatile precursors including salts are dissolved in a combustible liquid and processed in a spray flame. This approach enables the use of almost all elements and lowers the cost of raw materials compared to volatile metal-organic and organometallic precursors. Moreover, it provides the additional benefit that precursor mixtures can be used that in many cases predetermine the composition of multinary oxides. With appropriate process control, the production of materials with a defined composition, particle size, and morphology can be achieved.[2,3] Such materials are of great practical and

© Author(s) 2019

commercial interest in a wide range of applications, e.g., catalysis, battery storage, photovoltaic materials, and sensors. More than 600 publications issued in recent years describe the spray-flame synthesis of some 300 different materials[6,7,10–12] including multinary oxides such as perovskites.[13] Until now, however, only in few cases, spray-flame synthesis was transformed into larger-scale processes[10,11] due to the lack of detailed process understanding.

Central process steps such as the transfer of the dissolved substances from the spray droplets to the gas phase as well as the reaction and the interaction of the primary decomposition products with the flame are so far not sufficiently understood.[3] Various mechanisms of droplet disintegration including explosive evaporation[14,15] are discussed, and the competition between chemical reactions inside the droplet (that can also be supported by product water diffusing into the droplets) leads to the formation of mixed products, such formed in the liquid and such formed from evaporated constituents. In most cases, the latter are the desired product because they form nanoscale powders with adjustable characteristics, while the former lead to the formation of large-scale structures including solid or hollow spheres. Often, solvent mixtures are used to influence the evaporation process and to thus influence the materials properties.[16] Inhomogeneous mixing of the solvent with the surrounding oxidizing gas can lead to the local formation of hydrocarbon and carbon contamination. The high gas velocities required for atomization of the liquid initiate highly turbulent flows where the trajectories of individual volume elements can strongly deviate, thus leading to a broad distribution in the formed particle ensemble. Overcoming these hurdles requires a significant expansion of the understanding of the process chain of solution stabilization—spray formation and vaporization—interaction of precursors and metal atoms with the flame chemistry—and particle formation and growth in a complex turbulent reactive flow field.

The development of the currently existing methods of spray-flame synthesis was hitherto largely phenomenological with the focus on the characteristics of the materials produced. The approach was based generally on *ex situ* characterization of the materials and largely empirical variation of starting materials, reaction conditions, and burner geometries. This development was often decoupled from the advancement in related topics, in particular, combustion research, the spray formation, the interaction of precursors and fuels, solution stabilization and vaporization, diagnostics capabilities for reacting multiphase flows, and their numerical description. Therefore—despite the demonstrated successes—it is evident that through the synergetic use of the previous experience in the area of burner design, there is for the first time a realistic chance to overcome the obstacles mentioned above. Combining experimental experience from nanoparticle synthesis in premixed gas-phase systems and new *in situ* measurement methods with novel multiscale simulation approaches for reactive flows can significantly improve the mechanistic understanding of combustion processes. In the case of spray-flame synthesis, also new possibilities for the theoretical description of the properties of precursor solutions and solvents/solvent mixtures have to be considered.

Despite the popularity of spray-flame synthesis, the process was rarely investigated in computational fluid dynamics (CFD) simulations. The reason seems obvious: The process steps cover several spatial and temporal scales making the modeling and the numerical solution of the governing equations difficult. There is a high-speed jet of oxidizer gas that atomizes the liquid and transports the spray into the postflame atmosphere of a methane/oxygen pilot flame. The processes involved are barely understood; the evaporation processes and the combustion chemistry of the precursors are hardly known. Furthermore, there were hardly any detailed *in situ* measurements, which are a prerequisite for model- and code development and validation. Thus, the number of numerical studies is rather small. Gröhn presented simulations of zirconia synthesis from spray flames, validated by phase-Doppler anemometry (PDA) for spray characteristics and Fourier-transform infrared (FTIR) spectroscopy for flame temperature.[17,18] Weise investigated the process steps of titania synthesis in detail, from the primary spray break-up, up to the coupled modeling of the turbulent spray combustion and particle dynamics.[19] These simulations were based on Reynolds-averaged Navier-Stokes (RANS) equation models for the description of turbulence. Weise used direct simulations to obtain the spray characteristics, while Gröhn used boundary/initial conditions obtained experimentally. The first large-eddy simulation (LES) of the process was presented by Rittler[20] for the synthesis of silica. Here, the boundary conditions were obtained from the literature[21] and direct simulations. All three simulation cases suffered from similar difficulties: (a) the experimental database and its reproducibility were not sufficient for an exhaustive validation of the results and (b) the burner design necessitates strong simplifications and assumptions at the inlet boundaries. These problems were the main motivation for the design of a new, standardized, and easy to operate spray-flame synthesis burner and for the development of workflows to optimize the reproducibility of experiments.

In many research communities that investigate, e.g., aerosol diagnostics[22,23] and turbulent combustion, the coordinated use of standardized experiments (e.g., Gülder,[24] Santoro,[25] McKenna,[26] Taran,[27,28] Tsuji laminar burners,[29] TNF turbulent flames,[30] e.g., Sandia Flame D,[31] and ECN sprays[32]) enabled major progress in the development of chemical models, laser-based diagnostics, and simulation approaches. They work as an anchor for interdisciplinary research activities and lead to well-documented data bases with a long-term value. A well-designed burner that can be operated reproducibly in many laboratories under standardized conditions opens an ideal environment for a comprehensive experimental investigation as well as for the development and validation of models and simulation methods.

In the field of combustion synthesis of nanoparticles, no such approach existed so far. Therefore, experiments from different laboratories are not directly comparable even if they address the same materials system. Thus, differences in the results cannot be assigned to either differences in the setup, operating conditions, measurement protocols, or shortcomings of the models used for simulation. This work therefore aims at establishing a new standard spray-flame burner for nanoparticle synthesis called the SpraySyn burner.[3,33,34] A two-fluid nozzle disperses a flow of precursor solution via a high-velocity flow of O_2 that is stabilized by a surrounding axisymmetric premixed laminar CH_4/O_2 pilot flame. This pilot flame is surrounded by a coflow of N_2 to suppress the influence of the environmental conditions. The general approach follows the burner concept introduced by Kammler[1] that is also used in commercial apparatus, but the design has been modified and simplified for the purpose of linking detailed experiments with simulations. Important drivers of this redesign are the following:

© Author(s) 2019

- modular burner design that is easy to assemble and facilitates the exchange of spare parts to ensure operation under clean and reproducible conditions;
- alignment capability to generate symmetric flames;
- simulation-friendly geometry that prevents the time-consuming simulation of the periphery of the flame (e.g., locally high gas velocities in the pilot flame) and that is well documented;
- high flow rates to prevent the need for active cooling; and
- shielding against the environment.

A first milestone for the widespread utilization of the SpraySyn burner was reached in 2017 within the priority program SPP1980 of the German Research Foundation (DFG). By now, more than 16 SpraySyn burners are successfully installed in more than 12 laboratories to investigate the fundamentals of spray-flame synthesis. To ensure the correct and reproducible operation of the burner in every laboratory, we introduce a simple, standardized experiment for optical flame characterization that goes hand in hand with a unified postprocessing of the images that result in a flame benchmark. The required reference data are stored centrally in an open-access database that will contain an increasing amount of measured data and benchmark simulations.[35]

First, the schematics of spray-flame synthesis are explained using the conceptual burner design and initial simulations are presented that support the selection of the final burner dimensions and proportions required for stable operation. Consequently, the SpraySyn burner is introduced in detail, and standard operating conditions for nanoparticle synthesis are given. Because reproducible operation of a standard flame is crucial, an imaging-based flame characterization approach is introduced that enables each user to ensure the operation of the burner under comparable conditions.

II. EXPERIMENTAL

A. Schematics of the SpraySyn burner

The SpraySyn burner produces nanoparticles in a spray flame as illustrated in Fig. 1. The precursors are dissolved in a combustible liquid that is atomized by a two-fluid nozzle with external mixing via the difference in the relative velocities between the liquid and the O_2 dispersion gas.[36] The spray nozzle is surrounded by a laminar flat pilot flame that is stabilized on a porous plate. An inert gas coflow emanating from the same porous plate around the feed gases of the pilot flame has the role to stabilize the flame, to shield it against the environment, and to support the transport of the nanoparticles. With the appropriate selection of the precursor-solvent mixtures and the type and flow-rate of the gases, particle composition, size, and morphology can be controlled[1,7,37] and different nanostructures as well as nanocomposite materials can be produced. The final design and dimensions of the burner were selected based on experimental considerations supported by simulations and are introduced in Sec. III.

B. Simulation

The design of the SpraySyn burner was also motivated by the suitability for simulations, which require reproducible operation,

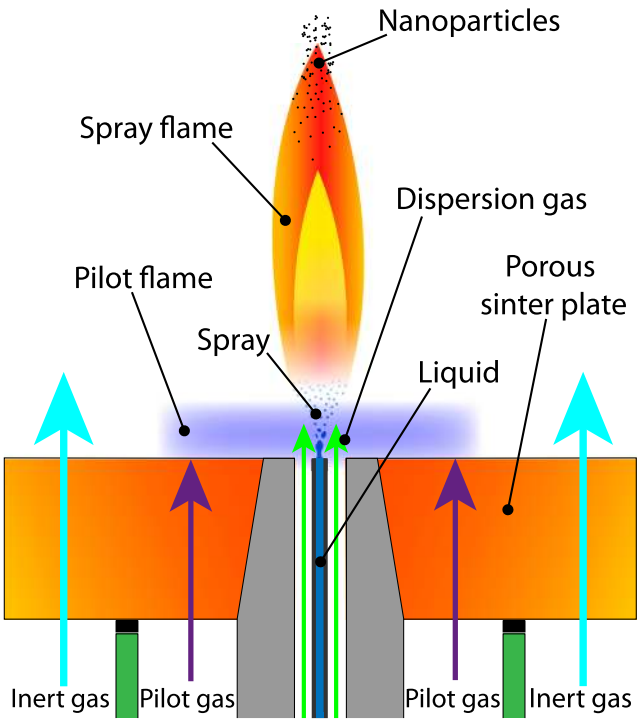

FIG. 1. Schematics of the spray-flame synthesis with the SpraySyn burner.

well-defined boundary conditions, and absence of unnecessary complexity that would otherwise consume most of the compute power and modeling effort. An example of unnecessary complexity would be a narrow annular slot for providing the fuel for the pilot flame. In the experiments, this slot would generate a high risk of flame asymmetry and for the simulations, it would require a very fine grid resolution for the description of the pilot flame. At the same time, these very fine cells would impose a stringent time step limit for the simulation, while requiring long initialization times to achieve a converged recirculation zone in the pilot flame. Therefore, the pilot flame was designed as a flat premixed flame stabilized on a porous matrix. As a result, it is nearly one-dimensional in the close vicinity of the burner matrix and can initially be modeled as a source of hot gases.

State-of-the-art in the simulation of turbulent flames is the large-eddy simulation (LES). It is best suited for numerical investigations of the spray-flame synthesis process as it describes the turbulent mixing well and resolves most of the turbulence-chemistry-aerosol-interactions that are still hard to model and could lead to large errors in RANS techniques.

In order to demonstrate the suitability of the SpraySyn burner for simulations, LES was performed using the in-house code PsiPhi.[38–41] The code relies on explicit time-stepping, cubic cells, low dissipative numerics (central differencing for momentum) in a conservative finite-volume formulation. Combustion is modeled using the PFGM (premixed flamelet-generated manifold) approach combined with artificial flame thickening (ATF), and subgrid viscosity is determined by Nichoud's sigma model.[20,42–44] The spray is described by Lagrangian particles.[20] The inlet plane of the simulation is located

© Author(s) 2019

TABLE I. Geometric features of the inlet boundary and inlet velocities.

	Inner radius (mm)	Outer radius (mm)	Inlet velocity (m/s)
Spray	0	0.75	91.34
Pilot	4	15	3.71
Coflow	15	35	0.637

where the primary spray breakup process is completed, few millimeters above the nozzle. The droplet-size distribution was assumed to be given by a Weibull distribution with 80% of the droplets having a diameter below 25 μm. This corresponds to a median diameter of approximately 21 μm and 90% of the droplets having a diameter between ~12.4 and 28 μm. However, measurements and detailed simulations of the primary and secondary droplet breakup should be performed and considered in future simulations.

The burner geometry can be described by the radii of the spray, pilot, and coflow inlets (Fig. 1). It must however be noted that the thickness and radial location of the mixing layer between the pilot and the coflow stream depend on the flow through the porous bronze matrix and thus on the respective mass flows. Hence, the dispersion gas flow and the spray boundary conditions must be known at the inlet of the computational domain. These boundary conditions will be provided by detailed experiments and simulations in the "SpraySyn project" but have been estimated for the initial simulations as shown in Table I.

Pilot combustion and spray-flame combustion are decoupled due to the simulation-friendly burner design so that the pilot flame could be described as an inlet-condition injecting burned gases. The pilot flame gases consist of methane and oxygen, while the spray is formed from ethanol atomized by oxygen (for details, see Table II). The simulations were performed on a domain of $150 \times 40 \times 40$ mm^3 discretized with 15.4×10^6 cells and a filter-size of 0.25 mm over 200 000 time steps for a real time of 0.2 s, taking two days on 1920 cores. Sampling was started after 0.1 s; a sampling time of 0.1 s should be sufficient for initial studies.

The detailed simulations confirm the design objective of the SpraySyn burner. The simulation-friendly geometry and the successful shielding against environment are of main interest. Figure 2 illustrates important features of the flame. Threshold values at $Z_{\mathrm{Pil}} = 90\%$ and $Z_{\mathrm{Et}} = 1.5\%$ have been chosen to guide the eye and delimit regions that are dominated by the off-gases from the pilot flame and by evaporated (but not yet burned) spray, respectively.

The hot products of the pilot heat up the spray and drive the droplet evaporation. The jet of dispersion gas causes the entrainment of the pilot gases toward the centerline, enhancing mixing and heating up. It should be noted that heat losses are not considered in the initial simulation so that the temperature and evaporation rate may be lower in the experiments. The source of the gaseous ethanol is located in the mixing layer between of the spray jet and the pilot, i.e., where the cold ethanol droplets are heated up by the hot gases.

Figure 3 shows cross sections of instantaneous and time-averaged flow and scalar fields of the SpraySyn flame. The axial velocity u is dominated by the jet of dispersion gas, while pilot gas velocities appear negligible. The pilot gas mixture fraction Z_{Pil} shows the large initial cross section of the pilot gas stream and how the pilot gases are entrained toward the centerline, being already merged with the jet after about 50 mm. The plot of the gaseous fuel mixture-fraction Z_{Et} confirms that most of the fuel mass emerge in the mixing layer between hot pilot flame gases and cold spray flame dispersion gas. Comparing the instantaneous mixture fractions Z_{Pil} of the pilot and the fuel Z_{Et}, it is apparent that most of the gaseous fuel stays within the pilot stream and that it is hardly lost to the cold coflow. This bodes well for nanoparticle formation, as the dissolved precursor is not likely to be lost to the cold coflow stream. The temperature map shows the dominant influence of the pilot flame and that the highest flame temperatures are reached in the pilot rather than in the spray flame. The evaporation source term dM shows the strongly localized evaporation rate around the Lagrangian fuel droplets and the smooth time-averaged evaporation rate fields, indicating that most of the evaporation is concluded after 25 mm. Interestingly, the largest evaporation rate is found within the first 5 mm on the centerline, despite the cold dispersion gas. This is because dM corresponds to the summed up evaporation contributions from individual droplets and therefore the high droplet flux density below 5 mm leads to the local maximum in the evaporation rate. Despite the high droplet flux density, the actual droplet density is rather low, due to the high dispersion-gas velocities. Due to the latter and the resulting velocity gradients, the droplet number concentration

TABLE II. Standard operating conditions of the SpraySyn burner. PF sets the standard conditions for the pilot flame, SF represents the conditions for the spray flame with ethanol (SF1), ethanol/ethylhexanoic acid (SF1-EHA), and the latter containing Fe(III)nitrate (SF1-Fe1). Further operating conditions can be found at www.spraysyn.org.[35]

Flow channel	Specification	PF1	SF1	SF1-EHA	SF1-Fe1
Pilot O_2	Gas, purity ≥ 99.5 mol. %	16 slm			
Pilot CH_4	Gas, purity ≥ 99.5 mol. %	2 slm	PF1		
Coflow N_2	Gas, purity ≥ 99.9 vol. %	120 slm			
Dispersion O_2	Gas, purity ≥ 99.5 mol. %	...	10 slm	SF1	
Liquid	Liquid, ethanol absolute (VWR Chemicals, No. 20821.330)	...	2 ml/min		SF1-EHA
	Liquid, 2-ethylhexanoic acid (Alfa Aesar, No. A12644)	...	...	35 vol. % ethanol/ 65 vol. % acid	
	Solid, iron(III)-nitrate nonahydrate ≥ 98% (VWR Chemicals, No. 24174.365)	...	...	...	0.05 mol/l in EtOH/EHA mixture

© Author(s) 2019

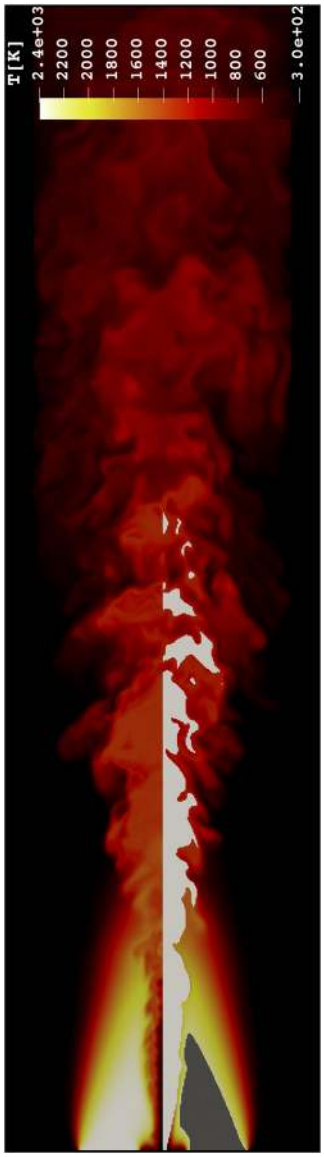

FIG. 2. Visualization of the flame structure. The dark gray surface depicts the region dominated by the pilot flame (mass fraction of pilot gases $Z_{Pil} > 90\%$), and the bright gray surface delimits the spray-dominated region ($Z_{Et} > 1.5\%$). Additionally, the temperature field is visualized following the color bar.

decreases above, leading to decreasing dM values. Overall, Fig. 3 provides evidence that the relevant features of the SpraySyn flame can be resolved with moderate grid resolutions and computational effort. The simulations show considerable levels of turbulence and thin mixing layers in the regions where nanoparticles are expected to be formed so that the nanoparticle concentration fields will fluctuate strongly in time and space, which must be considered in nonlinear formation and agglomeration terms by suitable modeling.

The present simulations for realistic synthesis conditions demonstrate the advantages of the SpraySyn burner design: Simulations can be performed efficiently on a compact computational domain, the flow field converges quickly, and a local refinement is not necessary in zones that are of no interest to spray-flame synthesis. Furthermore, boundary conditions can be specified at relative ease.

III. SPRAYSYN BURNER

A. Design

The final burner design shown in Figs. 4 and 6 was developed based on experience with the "flame spray pyrolysis" burner introduced by Kammler.[1] This burner features a thin annular slit as a flame holder for the pilot flame that provides the heat for evaporation and pyrolysis. To limit the mass flow from the pilot and avoid flashback, the gap has to be narrow so that symmetry is easily broken by manufacturing tolerance or thermal expansion during operation. Furthermore, the small gap requires an excessive resolution of the computational grid—away from the region of interest. To overcome these problems, the annular pilot was replaced by a flat and homogeneous flame and a finely adjustable atomizer nozzle. A porous bronze matrix (orange) with a planar surface and an outer diameter of 70 mm provides the homogeneous laminarized axisymmetric gas supply for the pilot flame (purple) and the coaxial coflow (light blue). The pilot flame is a premixed burner-stabilized methane/oxygen flat flame located around the central two-fluid nozzle in the center of the burner. To ensure a symmetric distribution of the coflow, the inert gas is supplied by a guide plate (yellow) located below the porous matrix. The guide plate has 20 equidistant slits resulting in a well-defined pressure drop that ensures a symmetric gas distribution. The gas flows feeding the pilot flame and the coflow are separated by a graphite flat seal. They are, however, intentionally allowed to mix and adjust in pressure within the porous plate downstream. This ensures a smooth transition in outlet velocities (in the range of 3.7 m/s for the pilot gasses and 0.64 m/s for the coflow) and a smooth variation in mixture ratio at the outer side of the pilot flame. Most importantly, it prevents the need of high grid resolution in this area and it prevents shear-flow interaction in between the two mixing fluids. All gas flows are metered by mass-flow controllers with flow rates shown in Table II for the respective standard operating conditions.

The spray is generated by a removable two-fluid nozzle with external mixing (Fig. 4, gray) in the center of the burner. The precursor solution is supplied via a metal capillary (inner diameter: 0.4 mm) with an exit velocity of ~0.26 m/s) that is surrounded by a high-velocity flow of O_2 as dispersion gas (green). The differences in the relative velocities between the liquid jet and the dispersion gas force a primary and secondary break-up and atomize the liquid into the desired spray.[36] To generate an upright and symmetric spray flame, the coaxial outflow of the dispersion gas has to be rotationally symmetric around the capillary. Therefore, the centric position of the capillary can be adjusted by 3 μm screws at the bottom of the burner housing. The liquid is supplied by a twin syringe pump that provides variable flow rates in the range from 0.1 to 5 ml/min and enables uninterrupted operation through alternating operation of the two syringes.

The various metal parts are sealed against each other and against the surroundings via a flat graphite seal and several O-rings

© Author(s) 2019

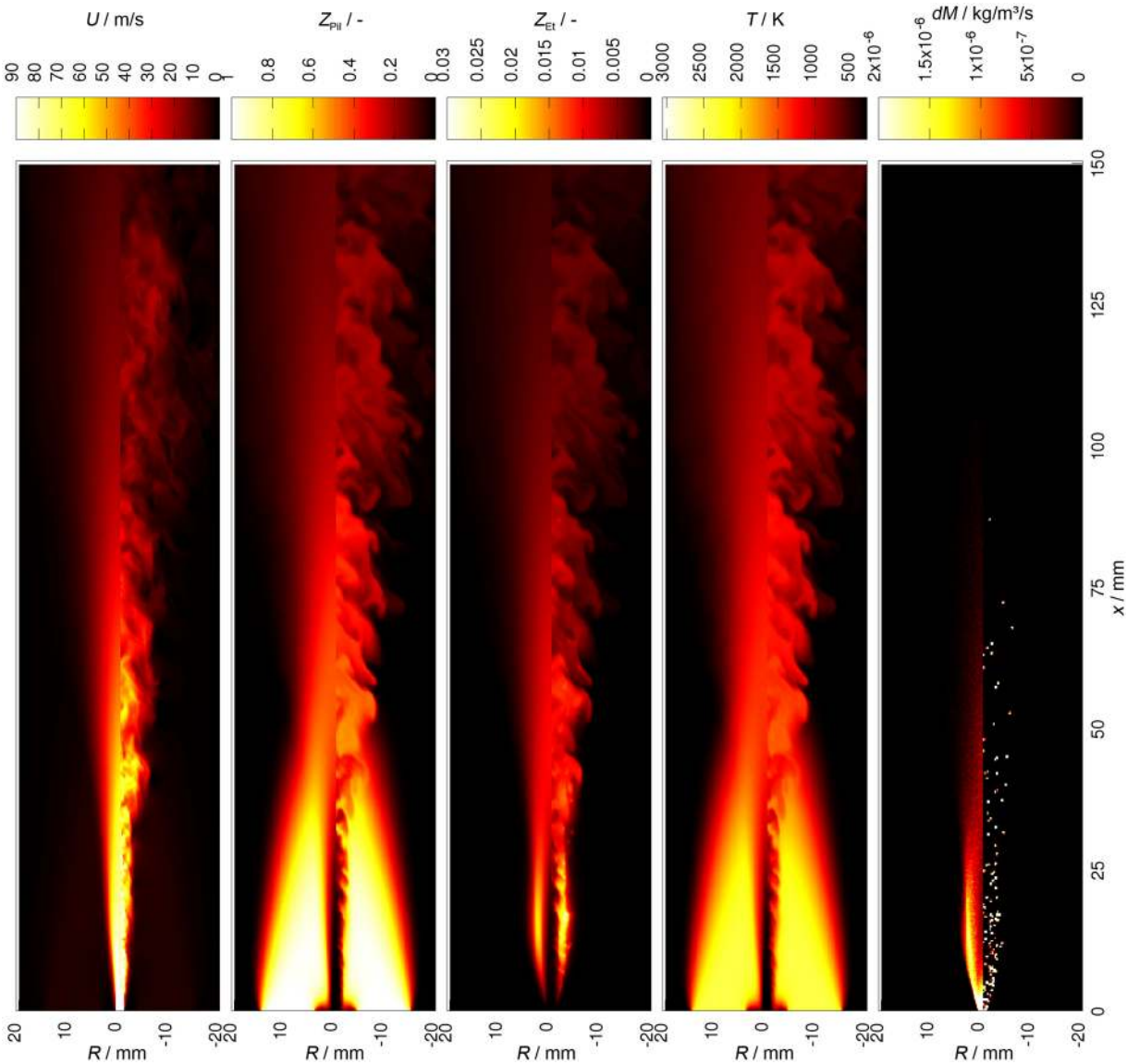

FIG. 3. Two-dimensional sections of (from left to right) axial velocity, pilot products mixture fraction, ethanol mixture fraction, temperature, and ethanol evaporation rate. Each plot consists of time-averaged (left) and instantaneous data (right).

to prevent an uncontrolled leakage and accumulation of the combustible pilot gas and to ensure a proper outflow of all gases. Due to the modular design of the burner, all burner components can easily be removed. This allows full access to all parts for cleaning or replacement of individual components with spare parts.

Figure 5 shows the completely assembled and ready-to-use SpraySyn burner. It has an outer diameter of 140 mm and can be mounted by six screws from the bottom to a closed reactor chamber (Fig. 6). The burner is designed for applications with the requirement of an optical access to the burner surface and the nozzle. Therefore, the mounting bolt circle and the sealing of the burner were constructed with a spatial offset to enable flush mounting with the inner surface of a closed reactor chamber. Independent of the mounting position, all connections and the micrometer screws are accessible from the bottom of the burner.

B. Operation

Table II presents one initial set of standardized operating conditions. For contributing to a consistent database,[35] it is recommended to perform measurements under these conditions.

For a reproducible use of the burner, it is not only important to operate the burner with well-controlled flow rates. It is also crucial to ensure the use of a clean matrix that features its original pore

© Author(s) 2019

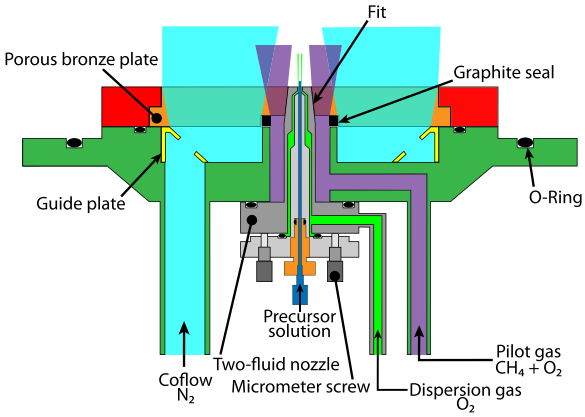

FIG. 4. Cross section of the SpraySyn burner.

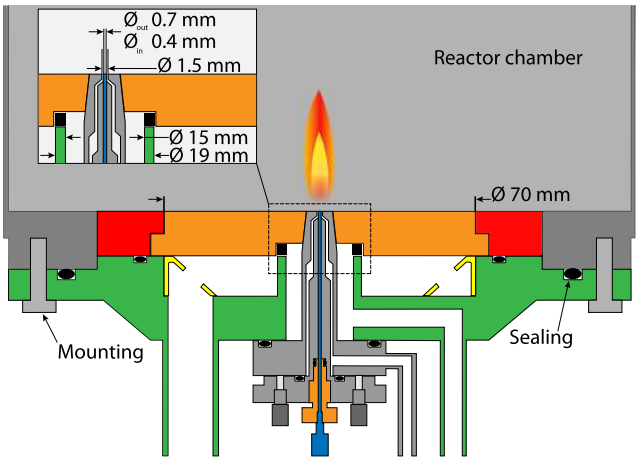

FIG. 6. Drawing of the SpraySyn burner mounted inside a reactor chamber. The SpraySyn burner is flush mounted and sealed from the bottom of a closed reactor chamber and can therefore be removed and serviced from the outside of the reactor.

structure and of a capillary without deposits. This, however, could be affected by (a) overheating the burner and (b) contamination with precursor solution and product. When operating the burner for the first time, the user will observe that the porous matrix oxidizes within the first minutes of operation. A dark, oxidized circular area will appear in the region of the pilot flame only and will not limit the aimed burner operation. However, to preserve the matrix structure over many operation hours, it is recommended to run the SpraySyn burner with a lean pilot flame to prevent excessive heating of the matrix. The light-off and shut-down protocol is important to prevent overheating and contamination of the burner matrix and the capillary. The recommended procedures are given in the Appendix. It is also recommended to regularly check the burner for its correct operation (see Sec. III C) and to eventually replace the porous plate and the capillary if deviations in the flame structure are recognized.

The correct assembling and handling of the burner leads to a reproducible and stable pilot flame named PF1 [Table II, Fig. 7(a)]. Pilot flame operation at a CH_4/O_2 equivalence ratio of $\phi > 0.25$ should be avoided, as the matrix will start to glow and change structure due to high temperatures. At $\phi < 0.125$, the pilot flame will blow off with the suggested flow rates. The pilot flame has a round, symmetrical shape and supports the spray flame SF1 properly. For operating the spray flame with ethanol or butanol, set the dispersion gas O_2 to 10 slm first and set the syringe pump to 2 ml/min second. Here, it is important to align the capillary into the center of the two-fluid nozzle by micrometer screws because a misalignment disturbs the symmetrical outflow of the dispersion gas and inhibits the proper atomization of the solvent. Once the alignment is finished, the ethanol/oxygen spray flame burns straight upward [Fig. 7(b)].

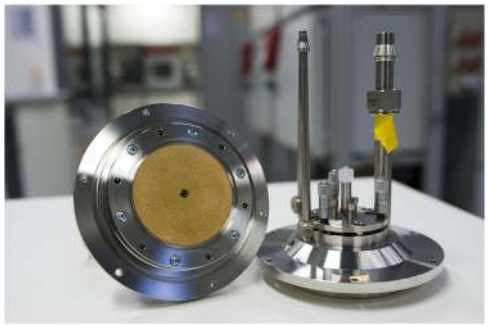

FIG. 5. Assembled and ready-to-use SpraySyn burners.

For nanoparticle synthesis, the spray flame can be operated with a large variety of liquid solvents (alcohols, acids, aliphatic and aromatic hydrocarbons, etc.) and molecular precursors such as HMDSO,[21,45] TEOS,[46,47] TTIP,[19,48] as well as carbonates[49,50] and nitrates[7,51] of various elements. In this work, we demonstrate the spray-flame synthesis of iron oxide nanoparticles based on $Fe(NO_3)_3$ nonahydrate dissolved in ethanol. To produce a stable solution in ethanol, it is necessary to provide an acidic environment, e.g., by addition of 2-ethylhexanoic acid. The spray flame consisting of a mixture of 35 vol. % ethanol and 65 vol. % acid [Fig. 7(c)] emits bright yellow light and is significantly wider and higher than the spray flame operated with pure ethanol. The precursor-laden flame [Fig. 7(d)] typically produces a mixture of iron oxide nanoparticles, containing maghemite (γ-Fe_2O_3), magnetite (Fe_3O_4), and hematite (α-Fe_2O_3).

Figure 8 (top) shows typical transmission electron micrographs for particles sampled from a filter placed in the off-gases of the reactor. The primary particles with a diameter of about 5–10 nm are partly sintered forming aggregates with sizes between 100 and 200 nm (left). High-resolution TEM (right) shows that the primary particles are crystalline. X-ray diffraction measurements (Fig. 8, bottom) show a main contribution from maghemite or magnetite (because of the almost identical crystallographic structure, these two phases cannot be separated based on their XRD patterns) and a small contribution from hematite (arrow at $2\theta = 33°$). The crystallite size obtained from the Rietveld refinement of the pattern (red graph) is about 7 nm, and a content of about 15% hematite

© Author(s) 2019

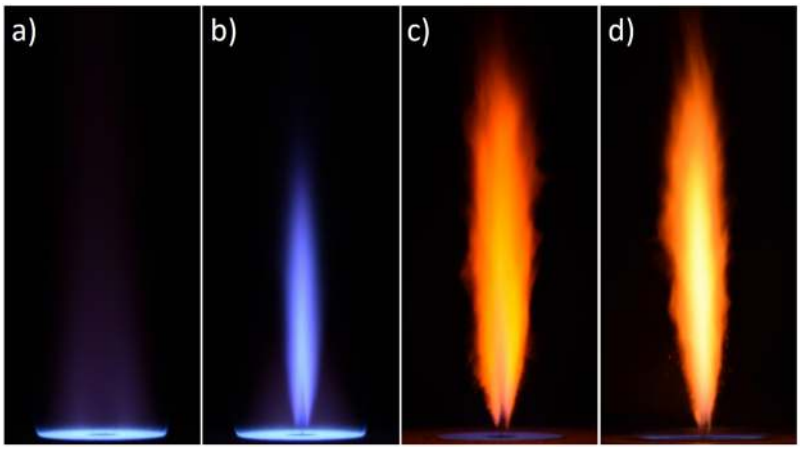

FIG. 7. (a) Pilot flame (PF1), (b) ethanol spray flame (SF1), (c) mixture of ethanol and 2-ethylhexanoic acid (SF1-EHA), and (d) Fe-III-nitrate spray (SF1-Fe1); (a) + (b) taken with an exposure time of 77 ms, (c) + (d) taken at 5 ms; for operating conditions (see Table II).

was calculated. This result is in good agreement with TEM and nitrogen adsorption (BET) measurements, where the respective mean particle diameter calculated from the specific surface area assuming monodisperse, spherical particles, is about 9 nm. The flame can further be influenced by secondary admixing of inert gases[52] or secondary reactants for particle coating.[53] However, the description of these modifications is beyond the scope of this manuscript.

C. Flame characterization

To ensure operation of the flame under standard conditions and to rule out adverse effects of deteriorated burner parts (porous plate or capillary), an imaging-based characterization method is introduced using a DSLR consumer camera and a MATLAB image postprocessing algorithm. Together, they enable the user to benchmark own results with the reference flames $PF1_{ref}$ [Fig. 7(a)] and $SF1_{ref}$ [Fig. 7(b)] regarding flame height, diameter, tilt angle, and flame color. Table III describes the recommended equipment and settings for flame imaging measurements that form the basis of the comparison and generate the correct data format for postprocessing. The use of other hardware as well as deviation from the suggested setup and postprocessing may lead to different evaluation results that make the comparison of the investigated flame with the reference flame pointless.

The SpraySyn target (Fig. 14, the Appendix) is positioned upright and centrally on the SpraySyn burner facing the camera. The camera body is placed horizontally at the same level as the upper

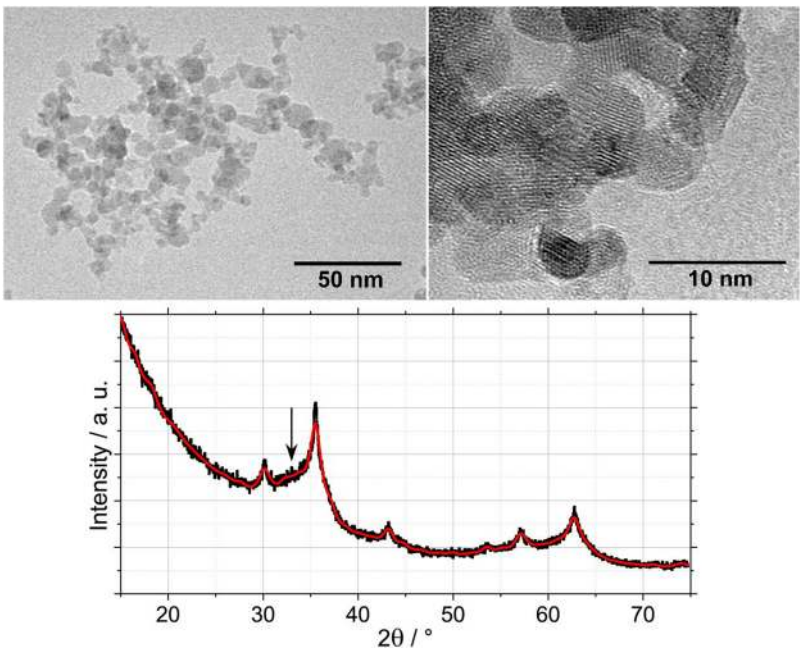

FIG. 8. Top: TEM image of iron oxide nanoparticles indicating agglomerates (left) and HR-TEM image showing an ensemble of crystalline iron oxide nanoparticles (right). Bottom: X-ray diffraction pattern of the as-synthesized iron oxides (black symbols) and Rietveld refinement of the measurement (red line). The black arrow indicates the signal that can be assigned to the hematite structure.

© Author(s) 2019

TABLE III. List of hardware and camera settings. Use manual mode M only; automated image correction must be disabled, e.g., active D-lighting, HDR, and special effects.

Camera	Nikon D5300 (Nikon item number VBA370AE, EAN 018208935543)
Lens	Nikon AF-S 50/1.8G Nikkor (Nikon item number JAA015DA, EAN 018208021994)
Resolution	24 megapixel, 14 bit
ISO	100
$f_\#$	1.8
Exposure time	1/13 s

surface of the SpraySyn burner at a distance of 700 mm between the camera chip and the front side of the target (Fig. 9).

For the flame characterization, a target image, background images, as well as about 50 images per flame (PF1 and SF1) are taken in a dark environment at the defined exposure times and f-stop settings given in Table III. A detailed tutorial, the MATLAB codes as well as the reference flame data for the flame benchmark can be downloaded from www.spraysyn.org. The postprocessing is based on the RAW images that are converted to 16-bit TIFF files using DCRaw[54] to make them accessible in MATLAB.[55] No gamma correction, color management, or white balancing is applied to the images. The TIFF images of the flame are checked for overexposure, and the background is subtracted subsequently. If the flames are operated under the standard conditions (Table II) and recorded with the given camera settings (Table III), there should be no overexposed image in the series.

The flame evaluation can be split into two parts. In part one, the flame geometry is characterized. Therefore, all three color channels of each image are summed up and radial intensity profiles are taken every 2 mm above the burner. A Gaussian fit is applied to each radial profile using a nonlinear least-square solver to determine the flame diameter by the FWHM of the Gaussian curve (Fig. 10).

The flame centerline is found by fitting a straight line through all peaks of the Gaussian profiles. Based on that, the flame height is calculated from the intensity distribution along the centerline for each image. The lower limit is preset to HAB = 0 and the upper limit,

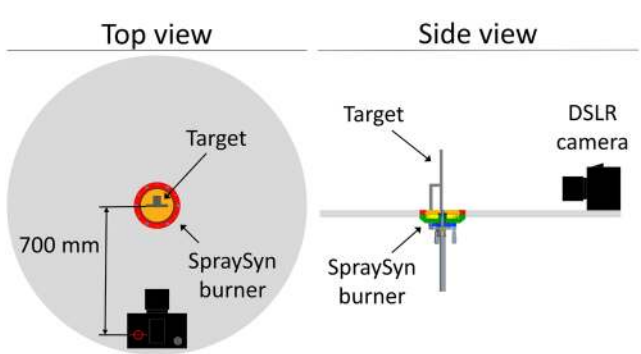

FIG. 9. Optical arrangement for flame characterization. A detailed manual that guides through the process of image acquisition and postprocessing is available at www.spraysyn.org.

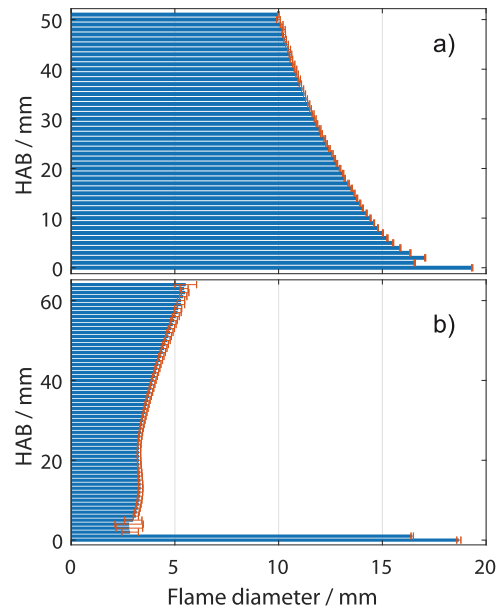

FIG. 10. Average flame diameter depending on height above the burner (HAB) for (a) $PF1_{ref}$ and (b) $SF1_{ref}$. The error bars show 2σ of the results from 200 images for $PF1_{ref}$ and 300 images for $SF1_{ref}$.

i.e., the flame height is preconfigured to an intensity threshold of 10% from the maximum counts along the centerline. Furthermore, the tilt angle is calculated between the flame centerline and a vertical line originating from $r = 0$ at HAB = 0. To keep the experiment simple, the tilt angle is evaluated from a single perspective only. To minimize the tilt angle, the user of the SpraySyn burner needs to align the capillary (Fig. 4) centrally in the two-fluid nozzle with the micrometer screws first, then optimize the position of the capillary slightly during operation of the spray flame aiming to adjust it as vertical as possible. The position of the camera should be chosen so that the flame is photographed from the perspective, from which the user observes the greatest angle of inclination, i.e., the camera position is orthogonal to the largest tilt angle. For closer inspection, users can take pictures from one to two additional perspectives to ensure correct alignment. Figure 11 shows the evaluated height and tilt angle of the reference flames. The resulting flame geometries (height, diameters, and tilt angle) are summarized in the characterized flame images (Fig. 12).

In part two of the flame characterization, the color information along the flame centerline is evaluated using the broadband flame chemiluminescence detected through the embedded Bayer filter of the DSLR camera. As the camera is part of the standardized experimental setup, the color profiles can directly be compared without further processing like color cross-talk correction.[56] Axial color profiles are taken along the flame centerline from the RGB images. A ratio of the blue and the red color channel C_{br} is used to evaluate the proper color distribution of the flame.

In the final flame benchmark, the flame characteristics evaluated by each user of the SpraySyn burner are compared with the reference flames $PF1_{ref}$ and $SF1_{ref}$. For that, the values of flame diameter and color ratio C_{br} are extracted at HAB = 10 mm for $PF1_{ref}$ and

© Author(s) 2019

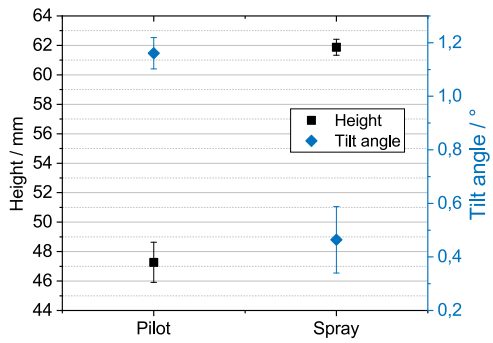

FIG. 11. Averaged flame heights and flame tilt angles for $PF1_{ref}$ and $SF1_{ref}$. The error bars show 2σ of the results from 200 images for $PF1_{ref}$ and 300 images for $SF1_{ref}$.

HAB = 20 mm for $SF1_{ref}$ that are known to be particularly sensitive to parameter variations for the respective flame. Figure 13 shows two example flame benchmarks, on the one hand for the pilot flame (a) and on the other hand for the ethanol spray flame (b).

In an ideal case, the deviation between the flame investigated (orange) and the reference flame (blue) would be zero at all four

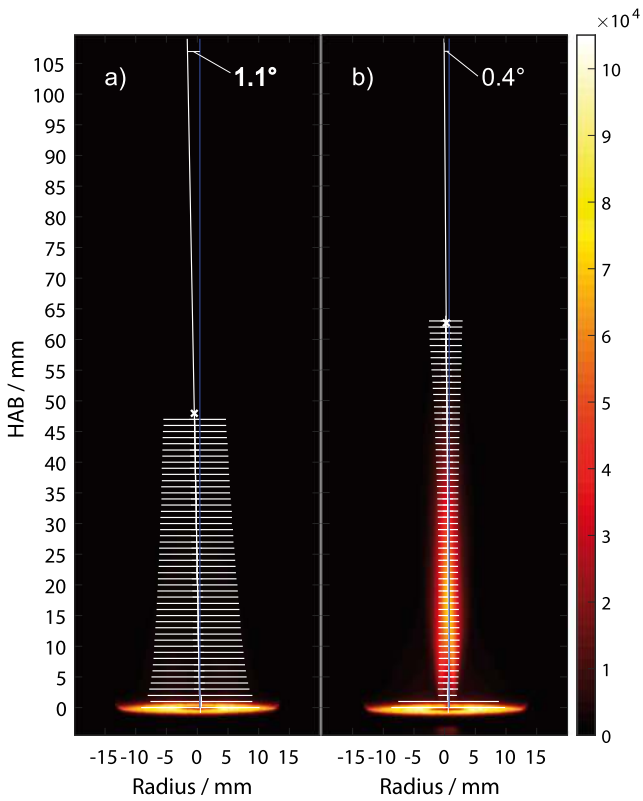

FIG. 12. Characterized flame images for (a) $PF1_{ref}$ and (b) $SF1_{ref}$ showing the flame diameters (horizontal lines), the flame height (white x), and the flame tilt angle derived from the flame centerline (white) and the corresponding vertical line (blue).

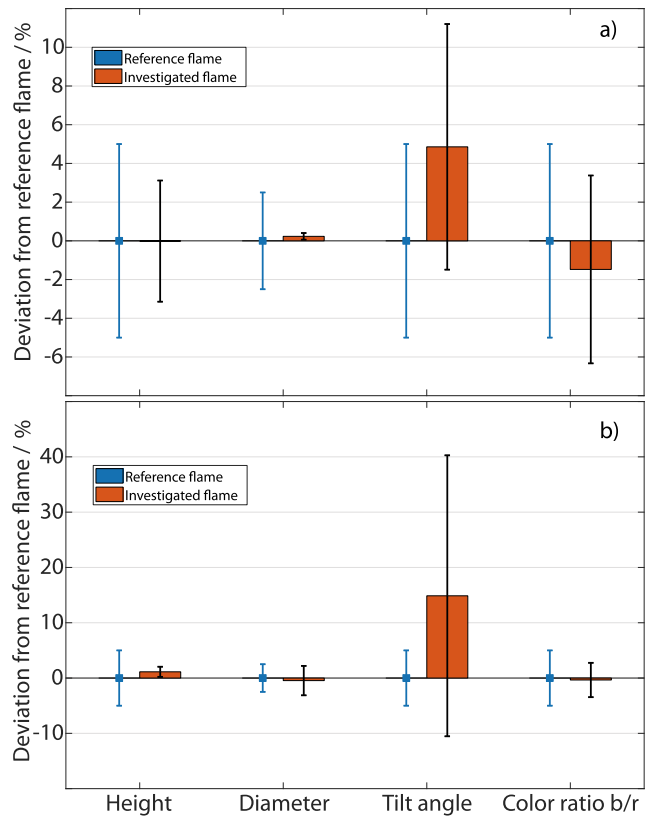

FIG. 13. Example flame benchmark of the investigated flames PF1 (a) and SF1 (b) performed by a user of the SpraySyn burner. The error bars of the reference flame (blue) indicate the given tolerances within that a flame operated by the user should rank to pass the benchmark successfully. The orange bars illustrate the relative deviations of the investigated flame from the reference flame indicating the calculated standard deviations by the black error bars.

criteria (height, diameter, tilt angle, and color ratio). In the given example, the height of the pilot flame [Fig. 13(a)] matches the height of the reference flame almost perfectly. In addition, the diameter of the pilot flame is only slightly larger compared to the reference flame, while the tilt angle is just within the specified tolerance of 5% (indicated by the blue error bars). The color ratio C_{br} of the investigated pilot flame is about 1.5% smaller compared to the reference flame, hence indicating that the investigated pilot flame emitted a slightly stronger red proportion in its broadband chemiluminescence. All in all, the investigated pilot flame passes the benchmark successfully that allows the user to perform the flame characterization of the ethanol spray flame.

The flame benchmark of the ethanol spray flame [Fig. 13(b)] shows that the investigated spray flame is about 1% higher than the reference flame. Regarding diameter and color ratio C_{br}, the investigated flame is slightly smaller and, again, slightly more red in contrast to the reference flame. Especially noticeable in this example is that the tilt angle is more than 12% greater compared to the reference flame. In this case, a readjustment of the capillary inside the nozzle of the SpraySyn burner is required and a new flame characterization

© Author(s) 2019

TABLE IV. Characterization results of the reference flames (www.spraysyn.org) for a SpraySyn burner operated without enclosure at an ambient temperature of 22 ± 2 °C and atmospheric pressure (1015 ± 8 mbar). The results are based on 200 images for $PF1_{ref}$ and 300 images for $SF1_{ref}$. Diameter and color ratio are extracted at HAB = 10 mm for $PF1_{ref}$ and HAB = 20 mm for $SF1_{ref}$.

	Height (mm)	Diameter (mm)	Tilt angle (deg)	Color ratio C_{br}
Reference flame $PF1_{ref}$	47.3	14.4	1.16	1.86
Reference flame $SF1_{ref}$	61.9	3.3	0.46	5.1
Tolerance (%)	5	2.5	5	5

should be performed by the user to assure comparable burner operation with regard to the reference flames. This way, comparability between results from different laboratories is enabled.

Beside the presented figures (Figs. 10–13), the provided MATLAB codes export the results of the flame characterization and benchmark in mat-files to provide the user with all relevant results highlighting if benchmark criteria exceed the given tolerances. Table IV summarizes the characterization results of the reference flames that are applied in the flame benchmark.

IV. CONCLUSIONS

In combustion research, standardized experiments have contributed significantly to bundling research from various research communities and gaining a detailed understanding of the processes. Without standard experiments, experimental and numerical data from various institutions are often inadequate or incompatible with one another or lack best-practice rules and possibilities for benchmarking. In the rapidly growing field of nanoparticle synthesis in flames, such an approach has so far been missing.

This paper introduces a standardized spray-flame burner for nanoparticle synthesis, SpraySyn. It has a modular structure and enables the generation of reproducible and symmetrical spray flames. A homogeneous, flat methane/oxygen pilot flame is stabilized by a nitrogen coflow. A precursor/solvent mixture is aerosolized and fed into the center of the hot burned-gas flow of the pilot flame as a spray by a two-fluid nozzle. This concept enables interdisciplinary research of fundamentals of spray generation, evaporation, flame temperature, species distributions, and nanoparticle formation and growth. The design of the SpraySyn burner is motivated by good accessibility to simulations which implies a simple formulation of boundary conditions for CFD simulations. The sophisticated pilot-flame design enables the use of the vast majority of the computational time for the calculation of the spray flame, as the pilot flame can be reduced to a heat source and its combustion products. LESs were demonstrated showing the successful shielding of the flame by the provided nitrogen coflow as well as a good prediction of the pilot flame and ethanol spray-flame geometry compared with experimental data. These well-defined and simulation-friendly boundary conditions and geometries of the SpraySyn burner are ideally suited for the development and validation of models and simulation methods. In particular, combination of the demonstrated simulation approach with state-of-the-art nanoparticle models is a natural next step.

To ensure intercomparability of experimental and numerical results between different laboratories, SpraySyn implies a simple, standardized optical setup for flame characterization based on quantification of the flame geometry and chemiluminescence detected by a consumer DSLR camera. All required components and settings are described, unambiguously, and standard operation parameters of the SpraySyn burner are presented. This also includes a light-off protocol and a comprehensive best-practice documentation of burner operation, disassembly, cleaning, and many more. A further component of SpraySyn is a uniform image postprocessing based on MATLAB scripts that are made available to the community. With the use of the suggested experiment together with the MATLAB scripts, both, pilot and spray flame, can be characterized in each laboratory and a benchmark with the reference flames $PF1_{ref}$ and $SF1_{ref}$ can be performed by each end-user of the SpraySyn burner. A growing database of experimental data as well as data about the computational domain is available at www.spraysyn.org.

ACKNOWLEDGMENTS

The authors gratefully acknowledge the funding by the German Research Foundation (DFG) within the priority program "Nanoparticle Synthesis in Spray Flames" SPP 1980 (Nos. 375220870 and 375857056). Our postprocessing script uses the following open-source functions from the MathWorks community: Export_fig by Yair Altman, GInput2 by Carlos Adrian Vargas Aguilera, NatSortFiles by Stephen Cobeldick, and Linspecer by Jonathan C. Lansey.

APPENDIX: OPERATION AND ANALYSIS GUIDELINES FOR THE SPRAYSYN BURNER

1. Light-off and shut-down protocol

The recommended steps to light-off the SpraySyn burner are described in Table V that ensure a gentle increase in temperature and prevent solid material from depositing on the matrix.

For shutting down the burner, the steps listed in Table VI are recommended to prevent contamination of the matrix and the capillary.

2. SpraySyn target

The target shown in Fig. 14 is recommended for taking photos of the pilot and spray flame with the DSLR camera following the steps described in the flame characterization section of this manuscript (a more detailed protocol is provided at www.spraysyn.org). The SpraySyn target has cross-shaped sections of three different sizes that allow the camera to focus, and four

© Author(s) 2019

TABLE V. Light-off protocol of the SpraySyn burner.

Step	Action
1	Set dispersion gas O_2 to 1 slm and make sure coflow N_2 is switched off
2	Set pilot O_2 and CH_4 to 0.5 slm each
3	Ignite the gases
4	Set coflow N_2 to 60 slm
5	Set coflow N_2 to 120 slm
6	Increase pilot O_2 in steps of 0.5 slm from 0.5 to 4 slm
7	Set pilot CH_4 to 1 slm
8	Increase pilot O_2 in steps of 1 slm from 4 to 8 slm
9	Set pilot CH_4 to 1.5 slm
10	Increase pilot O_2 in steps of 1 slm from 8 to 12 slm
11	Set pilot CH_4 to 2 slm
12	Increase pilot O_2 in steps of 2 slm from 12 to 16 slm
13	Set the dispersion gas O_2 to the desired level (10 slm for SF1)
14	Set the syringe pump to the desired level (2 ml/min for SF1)

rectangular markers that define the image section in the MATLAB postprocessing.

3. LES foundations

The set of equations that was solved consists of the transport equations of the Favre-filtered density $\bar{\rho}$, velocity $\tilde{u}$, mixture fraction Z, and progress variable Y_P,

$$\frac{\partial \bar{\rho}}{\partial t} + \frac{\partial \bar{\rho}\tilde{u}_i}{\partial x_i} = \dot{\Gamma}_{\bar{\rho}},$$

$$\frac{\partial \bar{\rho}\tilde{u}_i}{\partial t} + \frac{\partial \bar{\rho}\tilde{u}_i\tilde{u}_j}{\partial x_j} = -\frac{\partial \bar{p}}{\partial x_j} + \frac{\partial \bar{\tau}_{ij}}{\partial x_j} + \frac{\partial \tau_{ij}^{\mathrm{sgs}}}{\partial x_j} + \dot{M}_{d,i},$$

$$\frac{\partial \bar{\rho}\tilde{Z}}{\partial t} + \frac{\partial \bar{\rho}\tilde{u}_i\tilde{Z}}{\partial x_i} = \frac{\partial}{\partial x_i}\left(\bar{\rho}D_S\frac{\partial \tilde{Z}}{\partial x_i} + \dot{\Gamma}_{\tilde{Z}}\right),$$

$$\frac{\partial \bar{\rho}\tilde{Y}_\mathrm{P}}{\partial t} + \frac{\partial \bar{\rho}\tilde{u}_i\tilde{Y}_\mathrm{P}}{\partial x_i} = \frac{\partial}{\partial x_i}\left(\left[FED_\mathrm{p} + (1-\Omega)\frac{\mu_t}{\mathrm{Sc_t}}\right]\frac{\partial \tilde{Y}_\mathrm{P}}{\partial x_i}\frac{E}{F}\dot{\omega}_\mathrm{p} + \dot{\omega}_{\mathrm{p,evp}}\right)$$

with

$$Y_\mathrm{P} = Y_{\mathrm{CO_2}} + Y_\mathrm{CO}.$$

TABLE VI. Shut-down protocol of the SpraySyn burner.

Step	Action
1	Switch-off the syringe pump
2	Switch-off the dispersion gas O_2
3	Switch-off pilot CH_4
4	Switch-off pilot O_2
6	Wait 5 min to cool down the matrix and the burner housing
7	Switch-off coflow N_2

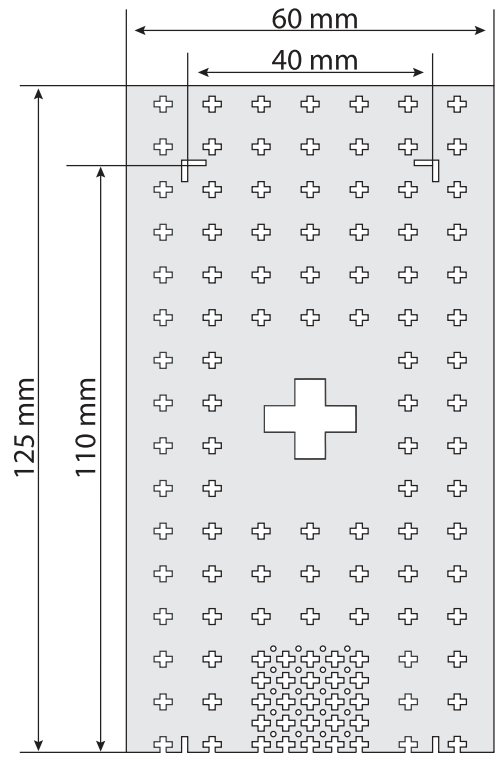

FIG. 14. Sketch of the SpraySyn target.

The pressure is considered by $\bar{p}$ and the momentum transfer from the droplet phase to the fluid by $\dot{M}_\mathrm{d}$. The viscous stress field is denoted by $\bar{\tau}_{ij}$ and the effect of the subgrid scale is modeled by the additional subgrid stress tensor τ_{ij}^{sgs} that can be calculated from the turbulent viscosity μ_t following the Nichoud's sigma model,[57]

$$\tau_{ij}^{\mathrm{sgs}} = \mu_t\left(\frac{\partial \tilde{u}_j}{\partial x_i} + \frac{\partial \tilde{u}_i}{\partial x_j} - \frac{2\partial \tilde{u}_k}{3\partial x_k}\delta_{ij}\right) \text{ with } \mu_t = \bar{\rho}(C_\mathrm{m}\Delta)^2 D_\mathrm{m}.$$

The turbulent viscosity depends on the model parameter C_m, the filter scale Δ, and the singular values of the G_{ij} tensor,

$$D_\mathrm{m} = \frac{\sigma_3(\sigma_1-\sigma_2)(\sigma_2-\sigma_3)}{\sigma_1^2} \text{ with } G_{ij} = \frac{\partial u_k}{\partial x_j}\frac{\partial u_k}{\partial x_i}.$$

The chemistry–turbulence interaction is described using the FGM (flamelet-generated manifold) framework combined with the ATF (artificial flame thickening) ansatz.[20,42–44] The transport equation of the mixture fraction Z evolution contains the source term due to spray evaporation $\dot{\Gamma}_{\tilde{Z}}$ and that of the progress variable Y_p is modified according to the ATF ansatz by introducing the thickening factor F, the efficiency function E, and the flame sensor Ω. The source terms representing the progress species' increase due to combustion and due to spray evaporation are $\dot{\omega}_\mathrm{p}$ and $\dot{\omega}_{\mathrm{p,evp}}$. In the current work, the mass fractions of CO and CO_2 are used for the definition of the progress variable.

© Author(s) 2019

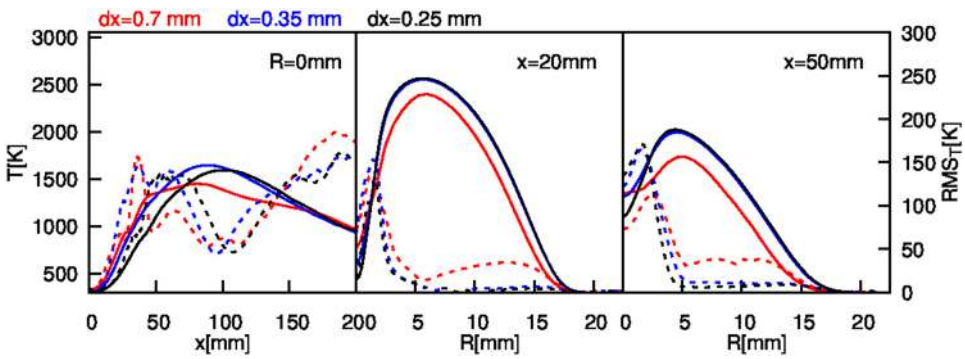

FIG. 15. Convergence of the temperature field with decreasing cell size.

The nanoparticle synthesis and growth are modeled by the sectional model,[58]

$$\frac{\partial \rho Q_k}{\partial t} + \frac{\partial \rho Q_k u_j}{\partial x_j} = \frac{\partial}{\partial x_j}\left(\rho D_k \frac{\partial Q_k}{\partial x_j}\right) + \rho \dot{\omega}_k^Q + \rho I \delta_{k1},$$

$$\dot{\omega}_k^Q = 0.5 \sum_{i=1}^{N_s} \sum_{j=1}^{N_s} \chi_{ijk} \beta_{ij} Q_i Q_j - \sum_{i=1}^{N_s} \beta_{ik} Q_i Q_k.$$

The evolution of the number densities of the individual size sections Q_k is controlled by the particles' diffusion coefficient in the size section k, the coagulation source term $\dot{\omega}_k^Q$, and the monomer nucleation term I. The coagulation source term itself is determined by the coagulation kernel β_{ij} that describes the frequency of collision between particles from sections i and j. The operator χ_{ijk} splits the volume of the coagulated particle between the sections, neighboring the particle's size.

The spray modeling is realized by a Lagrangian droplet description. Each droplet is characterized by its position x_d, velocity vector u_d, mass m_d, and temperature T_d. The corresponding evolution equations are given by[59,60]

$$\frac{dx_{d,i}}{dt} = u_{\mathrm{d},i}, \quad \frac{du_{\mathrm{d},i}}{dt} = a_{\mathrm{d},i} = \frac{\tilde{u}_i - u_{d,i}}{\tau_d} + \left(1 - \frac{\bar{\rho}}{\rho_\mathrm{d}}\right) g,$$

$$\frac{dm_\mathrm{d}}{dt} = \frac{\mathrm{Sh}}{3\mathrm{Sc}} \frac{m_\mathrm{d}}{\tau_\mathrm{d}} \ln(1 + B_m)$$

and

$$\frac{dT_\mathrm{d}}{dt} = \frac{\mathrm{Nu}}{3\mathrm{Pr}} \frac{c_p}{c_{p\mathrm{l}}} \frac{(T_g - T_d)}{\tau_d} \frac{\ln(1 + B_h)}{B_h} + \frac{\dot{m}_d L_v}{m_d c_{p\mathrm{l}}}$$

Here, τ_d is the characteristic time scale for momentum exchange between the fluid and the droplet and f_l a Reynolds number dependent correction factor. They can be calculated from the droplet density ρ_d, diameter d_d, and fluid viscosity μ via

$$\tau_d = \frac{\rho_\mathrm{d} d_\mathrm{d}^2}{18\mu}, \; f_\mathrm{l} = 1 + \frac{3}{20} \mathrm{Re}_\mathrm{d}^{0.687}.$$

The parameters are gravitational acceleration g, Sherwood number Sh, Schmidt number Sc, Prandtl number Pr, and the Spalding mass and heat transfer numbers B_m and B_h. The heat capacities at constant pressure for the fluid and droplet phase are denoted by c_p and $c_{p\mathrm{l}}$.

Prior to the decision for the cell size of 0.25 mm, a convergence study has been performed. Comparing the results for different cell sizes at Fig. 15 shows a satisfying convergence for the centerline ($R = 0$ mm) as well as for the two radial lines at $x = 20$ mm (evaporation) and $x = 50$ mm (combustion). The boundary conditions of the computational domain have been set as zero gradient at the inflow plane and constant value at the other planes.

REFERENCES

[1] H. K. Kammler, L. Mädler, and S. E. Pratsinis, Chem. Eng. Technol. **24**, 583 (2001).
[2] S. Kluge, L. Deng, O. Feroughi, F. Schneider, M. Poliak, A. Fomin, V. Tsionsky, S. Cheskis, I. Wlokas, I. Rahinov, T. Dreier, A. Kempf, H. Wiggers, and C. Schulz, CrystEngComm **17**, 6930 (2015).
[3] C. Schulz, T. Dreier, M. Fikri, and H. Wiggers, Proc. Combust. Inst. **37**, 83 (2018).
[4] S. Li, Y. Ren, P. Biswas, and S. D. Tse, Prog. Energy Combust. Sci. **55**, 1 (2016).
[5] M. Sokolowski, A. Sokolowska, A. Michalski, and B. Gokieli, J. Aerosol Sci. **8**, 219 (1977).
[6] L. Mädler, W. J. Stark, and S. E. Pratsinis, J. Mater. Res. **17**, 1356 (2002).
[7] W. Y. Teoh, R. Amal, and L. Mädler, Nanoscale **2**, 1324 (2010).
[8] A. Camenzind, R. Strobel, and S. E. Pratsinis, Chem. Phys. Lett. **415**, 193 (2005).
[9] R. Strobel and S. E. Pratsinis, J. Mater. Chem. **17**, 4743 (2007).
[10] H. Schulz, L. Mädler, S. E. Pratsinis, P. Burtscher, and N. Moszner, Adv. Funct. Mater. **15**, 830 (2005).
[11] L. Mädler, A. Roessler, S. E. Pratsinis, T. Sahm, A. Gurlo, N. Barsan, and U. Weimar, Sens. Actuators, B **114**, 283 (2006).
[12] R. Strobel and S. E. Pratsinis, Platinum Met. Rev. **53**, 11 (2009).
[13] B. Alkan, S. Cychy, S. Varhade, M. Muhler, C. Schulz, W. Schuhmann, H. Wiggers, and C. Andronescu, "Spray-flame-synthesized $LaCo_{1-x}Fe_xO_3$ perovskite nanoparticles as electrocatalysts for water and ethanol oxidation," ChemPhysChem (published online 2019).
[14] C. D. Rosebrock, T. Wriedt, L. Mädler, and K. Wegner, AIChE J. **62**, 381 (2016).
[15] C. D. Rosebrock, N. Riefler, T. Wriedt, L. Mädler, and S. D. Tse, AIChE J. **59**, 4553 (2013).
[16] S. Angel, J. Neises, M. Dreyer, K. Friedel-Ortega, M. Behrens, Y. Wang, H. Arandiyan, C. Schulz, and H. Wiggers, "Spray-flame synthesis of La(Fe, Co)O_3 nano-perovskites from metal nitrates," AIChE J. (published online 2019).
[17] A. J. Gröhn, S. E. Pratsinis, and K. Wegner, Chem. Eng. J. **191**, 491 (2012).
[18] A. J. Gröhn, S. E. Pratsinis, A. Sánchez-Ferrer, R. Mezzenga, and K. Wegner, Ind. Eng. Chem. Res. **53**, 10734 (2014).
[19] C. Weise, J. Menser, S. Kaiser, A. Kempf, and I. Wlokas, Proc. Combust. Inst. **35**, 2259 (2015).
[20] A. Rittler, L. Deng, I. Wlokas, and A. Kempf, Proc. Combust. Inst. **36**, 1077 (2017).
[21] D. Kilian, S. Engel, B. Borsdorf, Y. Gao, A. Kögler, S. Kobler, T. Seeger, S. Will, A. Leipertz, and W. Peukert, J. Aerosol Sci. **69**, 82 (2014).

© Author(s) 2019

[22] C. Schulz, B. F. Kock, M. Hofmann, H. A. Michelsen, S. Will, B. Bougie, R. Suntz, and G. J. Smallwood, Appl. Phys. B **83**, 333 (2006).
[23] H. A. Michelsen, C. Schulz, G. J. Smallwood, and S. Will, Prog. Energy Combust. Sci. **51**, 2 (2015).
[24] D. R. Snelling, K. A. Thomson, G. J. Smallwood, and Ö. L. Gülder, Appl. Opt. **38**, 2478 (1999).
[25] R. J. Santoro, H. G. Semerjian, and R. A. Dobbins, Combust. Flame **51**, 203 (1983).
[26] D. W. Senser, J. S. Morse, and V. A. Cundy, Rev. Sci. Instrum. **56**, 1279 (1985).
[27] K. Müller-Dethlefs and A. Schlader, Combust. Flame **27**, 205 (1976).
[28] K. Müller-Dethlefs, M. Péalat, and J. P. Taran, Ber. Bunsengesellschaft Phys. Chem. **85**, 803 (1981).
[29] H. Tsuji, Prog. Energy Combust. Sci. **8**, 93 (1982).
[30] See www.sandia.gov/TNF/abstract.html for information about standard turbulent flames in the context of the turbulent nonpremixed flames workshop.
[31] R. Barlow and J. Frank, Symp. (Int.) Combust. **27**, 1087 (1998).
[32] See https://ecn.sandia.gov/ for information about standard experiments in the context of the Engine Combustion Network.
[33] J. Menser, S. Kluge, H. Wiggers, T. Dreier, and C. Schulz, in Proceedings of European Combustion Meeting, Budapest, 2015.
[34] A. Abdelsamie and D. Thévenin, Proc. Combust. Inst. **37**, 3373 (2019).
[35] See www.spraysyn.org for details on SpraySyn burner standard operation.
[36] P. Walzel, Chem. Ing. Tech. **62**, 983 (1990).
[37] S. E. Pratsinis, Prog. Energy Combust. Sci. **24**, 197 (1998).
[38] T. Nguyen, P. Janas, T. Lucchini, G. D'Errico, S. Kaiser, and A. Kempf, SAE Technical Paper 2014-01-1121, 2014.
[39] A. Kempf, B. J. Geurts, and J. Oefelein, Combust. Flame **158**, 2408 (2011).
[40] F. C. Marincola, T. Ma, and A. Kempf, Proc. Combust. Inst. **34**, 1307 (2013).
[41] M. Pettit, B. Coriton, A. Gomez, and A. Kempf, Proc. Combust. Inst. **33**, 1391 (2011).
[42] A. Rittler, F. Proch, and A. M. Kempf, Combust. Flame **162**, 1575 (2015).
[43] G. Kuenne, A. Ketelheun, and J. Janicka, Combust. Flame **158**, 1750 (2011).
[44] F. Proch and A. M. Kempf, Combust. Flame **161**, 2627 (2014).
[45] S. R. Engel, A. F. Koegler, Y. Gao, D. Kilian, M. Voigt, T. Seeger, W. Peukert, and A. Leipertz, Appl. Opt. **51**, 6063 (2012).
[46] L. Mädler, F. Krumeich, P. Burtscher, and N. Moszner, J. Nanopart. Res. **8**, 323 (2006).
[47] R. Jossen, M. C. Heine, S. E. Pratsinis, S. M. Augustine, and M. K. Akhtar, Appl. Catal., B **69**, 181 (2007).
[48] W. Y. Teoh, L. Mädler, and R. Amal, J. Catal. **251**, 271 (2007).
[49] H. Schulz, W. J. Stark, M. Maciejewski, S. E. Pratsinis, and A. Baiker, J. Mater. Chem. **13**, 2979 (2003).
[50] M. Kim, T. R. Hinklin, and R. M. Laine, Chem. Mater. **20**, 5154 (2008).
[51] M. J. Height, S. E. Pratsinis, O. Mekasuwandumrong, and P. Praserthdam, Appl. Catal., B **63**, 305 (2006).
[52] R. Strobel, A. Alfons, and S. E. Pratsinis, Adv. Powder Technol. **17**, 457 (2006).
[53] A. Teleki, M. C. Heine, F. Krumeich, M. K. Akhtar, and S. E. Pratsinis, Langmuir **24**, 12553 (2008).
[54] See https://www.cybercom.net/~dcoffin/dcraw/ for Dave Coffin; accessed 2008.
[55] R. Summer, *Processing RAW Images in MATLAB* (University of California, Santa Cruz, 2014).
[56] J. Menser, F. Schneider, T. Dreier, and S. A. Kaiser, Exp. Fluids **59**, 373 (2018).
[57] F. Nicoud, H. B. Toda, O. Cabrit, S. Bose, and J. Lee, Phys. Fluids **23**, 085106 (2011).
[58] J. Loeffler, S. Das, and S. C. Garrick, Aerosol Sci. Technol. **45**, 616 (2011).
[59] B. Abramzon and W. Sirignano, Int. J. Heat Mass Transfer **32**, 1605 (1989).
[60] R. Miller, K. Harstad, and J. Bellan, Int. J. Multiphase Flow **24**, 1025 (1998).

© Author(s) 2019